Journal Name

Dynamic Article Links►

Cite this: DOI: 10.1039/c0xx00000x

www.rsc.org/xxxxxx

ARTICLE TYPE

Synthesis and lithium-storage properties of MnO/reduced graphene oxide composites derived from graphene oxide plus the transformation of Mn(VI) to Mn(II) by the reducing power of graphene oxide

Guixia Zhao,[a,b] Xiubing Huang,[b] Xiangke Wang*[a,c,d,e] Paul Connor,[b] Jiaxing Li,[a] Shouwei Zhang,[a] and John T.S. Irvine*[b]

Received (in XXX, XXX) Xth XXXXXXXXX 20XX, Accepted Xth XXXXXXXXX 20XX

DOI: 10.1039/b000000x

In this report, a novel method is proposed to prepare MnO/reduced graphene oxide(rGO) composites via calcining the precursors (i.e. δ-MnO_2/graphene oxide composites) at 500 °C in Ar using no external reducing gas, in which graphene oxide (GO) successfully serves as reductant by releasing CO during its thermolysis for the first time. By controlling the initial ratios of GO to $KMnO_4$, differently composed precursors can be obtained via the redox reaction between GO and $KMnO_4$, then leading to the formation of composites with different MnO/rGO ratios and dispersion of MnO on rGO surface (noted as MGC1 and MGC2). When applied as active materials in Lithium ion batteries, MGC1 shows excellent cycling performance and capacity retention. Under 100 and 200 mA g^{-1}, MGC1 could deliver reversible capacities as high as 900 and 750 mAh g^{-1}, respectively, after more than 100 cycles. Considering the simple operation and low energy consumption in the whole material synthesis processes, the present strategy is feasible and effective for the practical application. Even more importantly, the reductibility of graphene oxide upon thermolysis is utilized for the first time, which is meaningful for its extension in synthesis of functional nanomaterials.

With the increasing power and energy demand in portable electronic vehicles and devices, great efforts have been focused on developing new high-performance electrode materials for high-power rechargeable lithium-ion batteries (LIB).[1-5] Transition metal oxides, such as SnO_2,[6-8] TiO_2,[9] MoO_x,[10, 11] MnO_2,[12, 13] have been widely studied as anode materials in LIB since first proposed in 2000 by Poizot et al.[14] Among these transition metal oxides, manganese oxides (MnO_x) were a promising candidate series because of the relatively lower thermodynamic equilibrium voltage versus Li/Li^+,[15-17] and lower electromotive force,[18-20] as well as their environmental benignity and low cost. However, there are still several drawbacks such as: 1) the large volume change and gradual agglomeration of metal grains[21, 22] during the discharge/charge reaction; and 2) intrinsically low electronic conductivity, both of which result in the rapid fading of capacities during the cycling process.[23] To overcome these challenges, many researches were focused on the incorporation of carbon nanomaterials such as carbon nanotubes[24-26] and carbon nanofibers[27] with MnO_x to suppress the pulverization and capacity fading. After the discovery of graphene, more interest was paid on graphene/MnO_x nanocomposites for LIB with high capacity and long-life.[23,28-30] However, many of these composites were synthesized under severe conditions and usually needed higher cost for the calcination. For example, in Sun et al.'s report, by mixing $Mn(CH_3COO)_2$ and GO solutions, and adding hydrazine hydrate, a Mn-precursor/graphene intermediate was obtained, which was then annealed at 500 °C in 5% H_2/Ar atmosphere for 5 h to obtain the final MnO/graphene composite.[31] Similar strategy was used for N-doped MnO/graphene hybrid by calcining a precursor, i.e. Mn_3O_4/graphene, at 800 °C for 5 h under NH_3 atmosphere.[32] In Qian's group, the precursors MnOOH nanowires were first synthesized through hydrothermal procedure and after the following calcination in air, Mn_2O_3 nanowires were obtained. The final MnO@C core-shell nanowires were produced by exposing these Mn_2O_3 nanowires to argon and an acetylene/argon gas mixture at 500 °C.[33]

Different from many of the reported work, we herein introduced MnO/rGO composites via a quite different synthesis approach. As reported in many publications,[34, 35] theoretical and experimental proofs have proved that thermal reduction of graphene oxide would release CO and CO_2, and the CO-CO_2 ratios were dependent on the thermal conditions. Therefore, in this work, we tried to utilize the reductive CO released from GO to in-situ reduce MnO_2 in the MnO_2/GO composites to obtain MnO/rGO composites without using any external reductive gases, such as H_2 and CO, which makes the synthesis process with less cost and more safety. What's more important, GO is utilized as solid reductant for the first time and this valuable finding will arouse more interest in the GO research for material synthesis. In our previous research, it has been proven that the mild redox reaction between graphene oxide and $KMnO_4$ would result in

highly active δ-MnO_2 nanosheets.[36] In the present work, by adjusting the ratio of graphene oxide and $KMnO_4$, different contents of graphene oxide can be retained in the δ-MnO_2/graphene oxide composites. As shown in Figure 1, we typically tried three different weight ratios between $KMnO_4$ and graphene oxide. The redox reaction between the two reactants, resulted in three precursors, P-MNP, P-MGC2 and P-MGC1. Through the further calcination under Ar at 500 °C, δ-MnO_2 in the precursors (P-MGC2 and P-MGC1) can be reduced into MnO due to the reductive gas (CO) released out from the thermolysis of graphene oxide, resulting in the formation of MGC2 and MGC1. No graphene oxide was found in the P-MNP, so that after the calcination under Ar at 500 °C, δ-MnO_2 was transferred to α-MnO_2 nanoparticles (noted as MNP). The general synthesis process for these manganese oxides and their hybrids with graphene is illustrated in Figure 1 (see more experimental details in Supporting information).

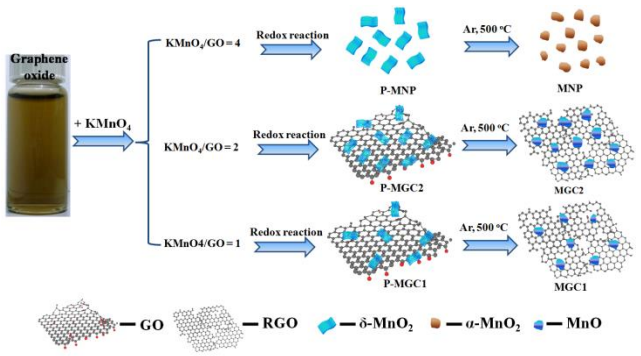

Figure1. Schematic diagram on the formation of manganese dioxide nanoparticles (MNP) and manganese monoxide/rGO composites (MGC1 and MGC2). The preparation included first synthesis of the precursor, i.e. P-MNP, P-MGC1 and P-MGC2 through the controllable redox reaction between graphene oxide and $KMnO_4$. Then the final materials were obtained by calcination of the precursors under Ar at 500 °C for 90 minutes.

Results and Discussion

The precursors resulting from the redox reaction between graphene oxide and $KMnO_4$ were found to contain δ-MnO_2 with a monoclinic birnessite (containing K) phase from the XRD (Figure SI1, Supporting Information), similar to our reported results. And the TGA results in air (Figure SI2a-c, Supporting Information) showed that no graphene oxide was remaining in P-MNP, while for P-MGC2 and P-MGC1, it can be implied that the remaining graphene oxide contents were about 14% and 37%, respectively, by calculating the mass loss during the heating in air. After annealing these precursors at 500 °C for 90 min under Ar atmosphere, different manganese oxides were obtained. Figure 2 shows the XRD patterns of MGC1, MGC2 and MNP. It is obvious that MNP (Fig. 2c) is indexed to a pure α-MnO_2 phase with a tetragonal crystal system (JCPDS no. 44-0141), while MGC2 (Fig. 2b) and MGC1 (Fig. 2a) readily correspond to a cubic phase of MnO (JCPDS no. 07-0230), and their TGA analysis in air indicate that rGO contents are about 18% and 39%, respectively (Figure SI2d-f, Supporting Information).

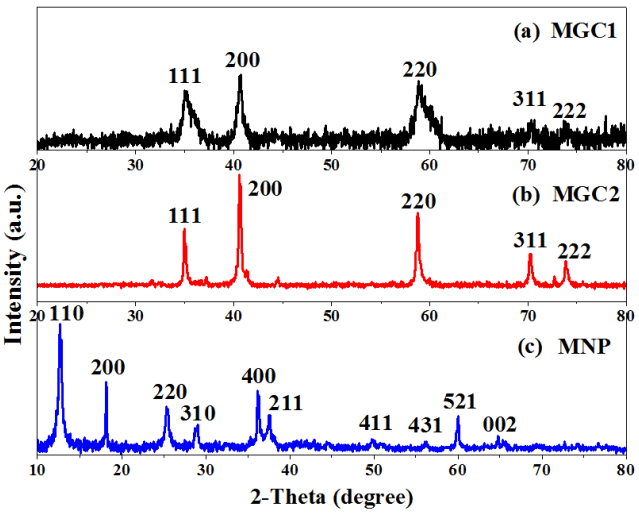

Figure 2. X-ray diffraction (XRD) patterns of (a) MGC1, (b) MGC2 and (c) MNP.

The high-resolution X-ray photoelectron spectroscopy (XPS) analysis is shown in Figure 3a. The peaks at around 640 and 651 eV for MGC2 and MGC1 are attributed to Mn(II) $2p_{3/2}$ and $2p_{1/2}$, respectively,[37] which are quite different from the peaks for MNP located at about 642 and 653 eV, the characteristics of Mn(IV).[38] Raman spectra were carried out to further identify the structure and constituent of MNP, MGC2 and MGC1, as presented in Figure 3b. The characteristic D band and G band of carbon materials are present in MGC2 and MGC1, but absent in MNP, further indicating that there is no graphene in MNP. Additionally, the peaks at around 580 and 650 cm^{-1} for MGC2 are assigned to manganese oxide.[39-41] In the sample MGC1, there is only one peak around 650 cm^{-1} for MnO, which may be due to the fact that the signal intensity for the metal-oxygen bond is usually lower than the D and G band for rGO. And in MGC1, the graphene content is higher than that in MGC2, so the D and G peak intensity is even much higher than that for metal-oxygen bond. As a result, the peak 580 cm^{-1} is not as obvious as the 650 cm^{-1} in MGC1.

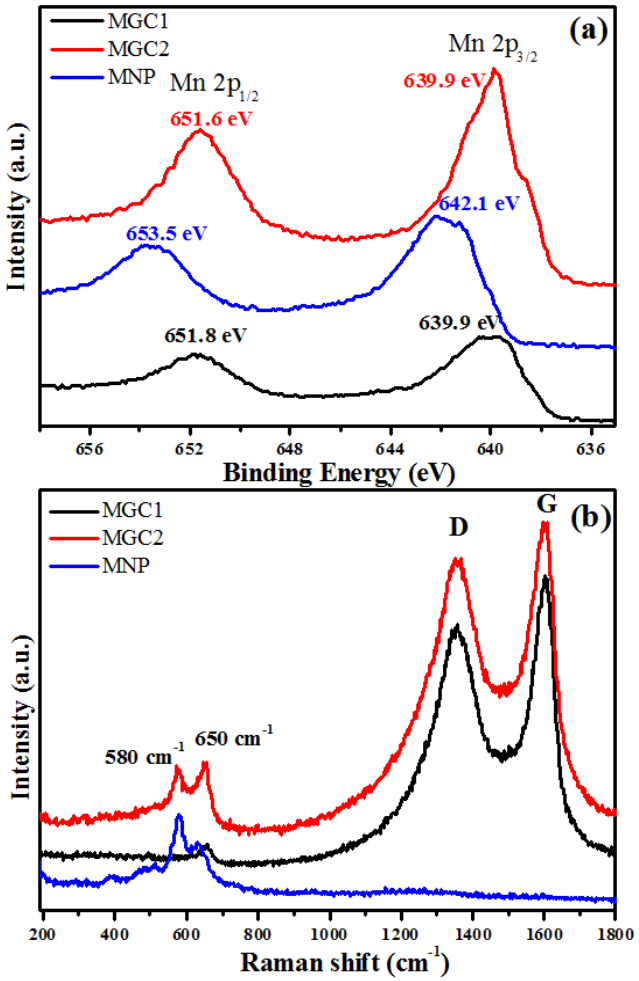

Figure 3. High-resolution Mn 2p XPS spectra (a) and Raman spectra (b) for MGC1, MGC2 and MNP

Figures 4, 5 and 6 show the typical SEM and TEM images of MNP, MGC2 and MGC1, respectively. Evidently, α-MnO_2 nanoparticles in MNP are well dispersed with the size of about 50 nm with a narrow size distribution (Fig. 4a and c). For MGC2 and MGC1 as shown in Figs. 5 and 6, MnO nanoparticles are both with a size of ca. 50 nm, and it is also obvious to note that the graphene content in MGC2 is lower than that in MGC1, which makes more aggregation of MnO in MGC2 while MnO nanoparticles in MGC1 are well dispersed on the surface of rGO. The high-resolution TEM (HRTEM) images of MGC2 (Fig. 5d) and MGC1 (Fig. 6d) showed the interplanar distance of ca. 0.25 nm, corresponding to the (111) plane of cubic MnO. The FFT (Fast Fourier Transform) patterns inset in the HRTEM images also show the spot pattern representative of crystalline phase, although the intensity is quite low due to the low crystallinity of MnO nanoparticles. However, MNP showed a different lattice spacing of ca. 0.48 nm (Fig. 4d), which corresponds to the (200) plane of α-MnO_2. The N_2 adsorption-desorption isotherms (see Figure SI3, Supporting Information) also showed a higher BET specific surface area of MGC1 (46.3 m^2/g) than that of MGC2 (27.4 m^2/g).

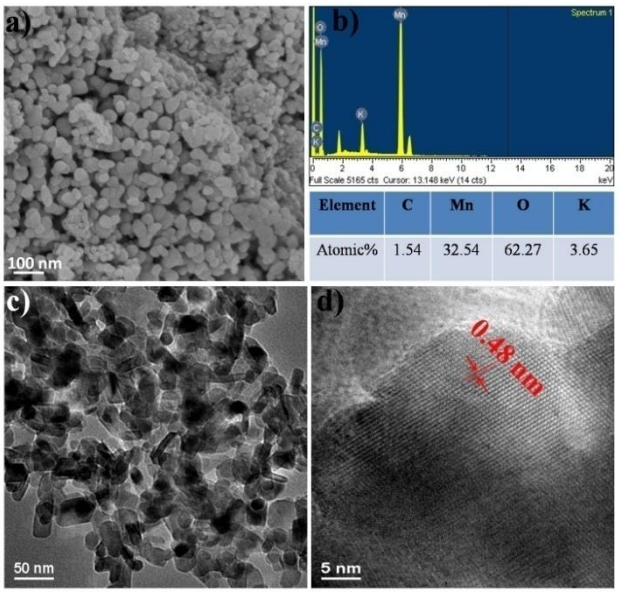

Figure 4. (a, b) SEM images and corresponding Energy Dispersive Spectra (EDS) of MNP; (c, d) TEM and HRTEM images of MNP

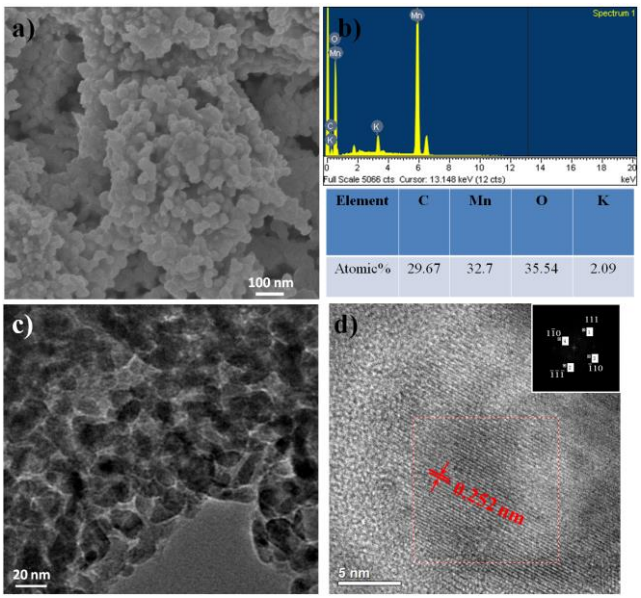

Figure 5. (a, b) SEM images and corresponding Energy Dispersive Spectra (EDS) of MGC2; (c, d) TEM and HRTEM images of MGC2 (the inset in d shows the FFT pattern with marked spots)

The energy-dispersive spectra (EDS) also indicate the existence of Mn, O and C in MGC1and MGC2. The rough atom ratio of Mn to O is about 1:1 and the atom ratios of C to Mn are also consistent with the previous analysis. For MNP, the rough atom ratio of Mn to O is about 1:2 and the little signal (about 1.5 atom%) for carbon may come from the environment or adsorbed CO_2. From the above analysis, by increasing the initial ratio of graphene oxide to $KMnO_4$ in the redox reaction, the more graphene oxide can be remain in the resulting δ-MnO_2/GO composites (pure δ-MnO_2, i.e. P-MNP was obtained when the weight ratio of $KMnO_4$ to GO was 4:1). During further heating treatment under Ar atmosphere, the carbon in graphene skeleton

can't reduce MnO_2 since the temperature is only 500 °C.[42] The remaining graphene oxide undergoes thermolysis to release CO and CO_2, as reported by many researchers.[34, 35] Thus, even in the inert atmosphere, MnO_2 can be reduced into MnO, which is decorated on the graphene support and the remained graphene oxide is also reduced to rGO at the same time. This is quite different from results reported by Sun et al.,[31] where Mn^{2+} was used as Mn source and H_2/Ar was used as reductive gas for graphene oxide. For P-MNP, no graphene oxide containing means no CO releasing out, so α-MnO_2 nanoparticles were obtained because of the phase change of δ-MnO_2 into α-MnO_2 during high-temperature treatment. Summarily, in this work, the reducting power of graphene oxide has been successfully proven and used to prepare MnO from MnO_2 without any extra reductants.

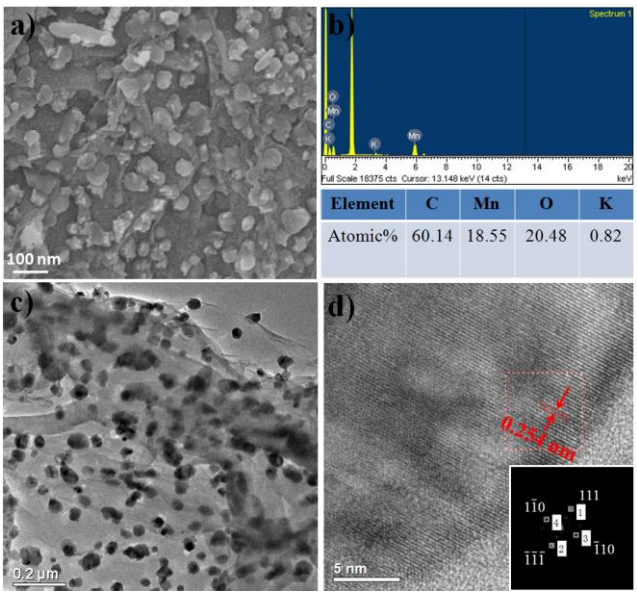

Figure 6. (a, b) SEM images and corresponding Energy Dispersive Spectra (EDS) of MGC1; (c, d) TEM and HRTEM images of MGC1 (the inset in d shows the FFT pattern with marked spots)

The electrochemical lithium-storage performance of the as-prepared MnO/rGO composites was also investigated. The galvanostatic discharge/charge cycling performance was tested at a current of 100 mA g^{-1} with a voltage window of 0.05-3.5 V. As shown in Fig.7a, for a current density of 100 mA g^{-1}, the first discharge capacity of MGC1 was over 1800 mAh g^{-1}, and the initial capacity loss is about 50%, which is believed due to the disordered rGO and the trap sites for Li on its surface to form SEI. Interestingly, in the following cycling, the capacity increased gradually and stabilized at 900 mAh g^{-1} after 85 cycles. The capacity rise has been reported in many published works and was considered to be attributed to a possible activation process in the electrode.[31, 33] The initial capacity has a significant irreversible component; however, capacity in subsequent cycles is of similar order to that expected for Mn^{2+}/Mn^0 conversion. On a number of cycles the capacity exceeded that expected for just the Mn couple and may possibly reflect a component due to the organic polymeric/gel like films formed reversibly by decomposition at low potential.[33, 43] According to the theoretical overall reaction between lithium and graphene nanosheets, $2C + Li^+ + e^- \leftrightarrow LiC_2$ (with a capacity of 1116 mAh g^{-1})[44-46] and the theoretical conversion of MnO and Li, $MnO + 2Li^+ + 2e^- \leftrightarrow Li_2O + Mn$ (with a capacity of 756 mAh g^{-1}),[46] as well as the content analysis of the composite through TGA shown in Fig. SI2d-f, the theoretical capacity for MGC1 is about 896 mAh g^{-1}, which is in good agreement with the stable capacity of 900 mAh g^{-1} after 85 cycles at a low current density of 100 mA g^{-1}.

In the following rate capability test at various current densities, discharge capacities of 750 mAh g^{-1}, 580 mAh g^{-1}, 400 mAh g^{-1} and 160 mAh g^{-1} were retained at current densities of 200 mA g^{-1}, 400 mA g^{-1},800 mA g^{-1} and1.6 A g^{-1}, respectively. It seems that the rate performance is not as high as that of other reported carbon-MnO materials.[31, 33] For the MnO/graphene prepared by Sun et al., the reversible capacity is high up to 2014.1 mAh g^{-1} at a current of 200 mA g^{-1} and 625.8 mAh g^{-1} at a current of 3000 mA g^{-1}.[31] Also according to Li et al., MnO@C electrode delivered a capacity of 861 mAh g^{-1} at a current of 100 mA g^{-1} and 462 mAh g^{-1} at a current of 2000 mA g^{-1}.[33] The relatively low rate capability may be ascribed to the relatively lower electronic conductivity of reduced graphene oxide in the active material that results in the incomplete discharge/charge process at high current densities. However, importantly, the capacity was able to recover to more than 900 mAh g^{-1} after 120 cycles when the current density was returned to 100 mA g^{-1}. More details in the discharge/charge process can be seen from the discharge/charge voltage profile in Fig.7b, which showed a discharge plateau at ca. 0.31 V in the 1st cycling and a shifted plateau at ca. 0.42 V in the later cycling. It also showed a charging plateau at ca. 1.2 V and in the further cyclings, from 16th to 85th cycling, another small charge slope gradually broadened, which was in agreement with the increased capacities in the discharge/charge process.

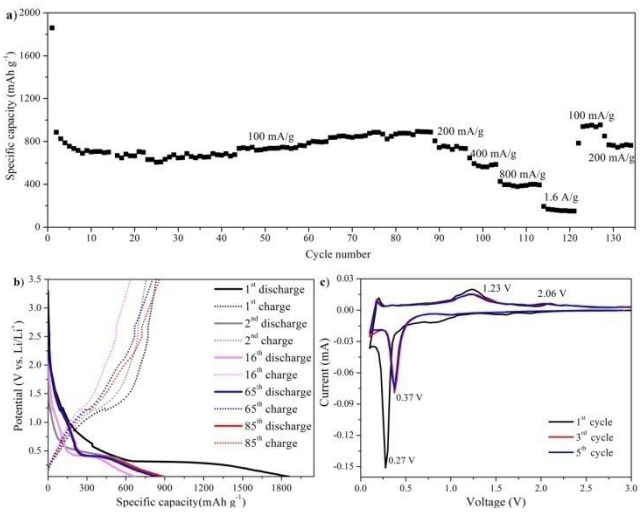

Figure 7. a) Cycling performance of MGC1 at various current densities; b) Discharge/charge voltage profiles of MGC1 at a current density of 100 mA g^{-1}; c) Current vs. Voltage profiles frompotentialstatic discharge/charge cycle of MGC1.

Fig. 7c shows the potentiostatic discharge/charge cycling behavior of MGC1 electrode. In the first discharge, a sharp

cathodic peak at about 0.27 V was considered due to the complete reduction of Mn(II) to Mn(0), and this peak shifted to 0.37 V in the following cycles, which was supposed due to the improved kinetics and the alternated microstructure of the MGC1 electrode after the first cycle.[48-50] In the 1st anodic process, the peak at ca. 1.23 V was ascribed to the oxidation of Mn(0) to Mn(II), which also remained at 1.23 V in the subsequent cycles. It is noted that there is another small oxidation peak at ca. 2.06 V, which is quite stable with cycling. This peak also appeared in many previous studies on MnO/graphene and MnO_x/carbon electrodes and it is considered due to the fact that Mn(II) could be re-oxidized to higher oxidation state with the aid of fast Li reaction kinetics and the synergistic effects of carbon and MnO_x.[31, 51-53, 42,44-45] It is worth noting that the second and onward cycling CV curves remained almost unchanged, indicating the relatively stable discharge/charge process with good chemical reversibility.

For the other MnO/rGO composites (i.e. MGC2) as shown in Fig. 8a, the capacity and rate capability are not as good as MGC1. Under a current of 100 mA g^{-1}, the stable discharge capacity was about 400 mAh g^{-1}, while at higher currents of 200 mA g^{-1}, 400 mA g^{-1}, 800 mA g^{-1} and1.6 A g^{-1}, only 380 mAh g^{-1}, 270 mAh g^{-1}, 170 mAh g^{-1} and 20 mAh g^{-1} were remained, respectively. When the current density went back to 100 mA g^{-1}, the stable capacity was only recovered to 300 mAh g^{-1}. It is easy to discern that MGC2 did not experience any increase in the capacity performance. From the discharge/charge voltage profile in Fig. 8b, it is also noted that only one charge slope located at ca. 1.2 V, although the discharge slope location in the whole cycling is similar with that of MGC1.

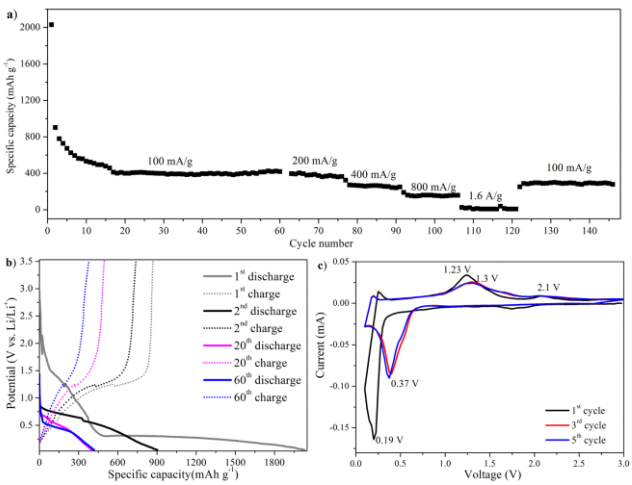

Figure 8. a) Cycling performance of MGC2 at various current densities; b) Discharge/charge voltage profiles of MGC2 at a current density of 100 mA g-1; c) Potentialstatic Current vs. Voltage profiles of MGC2.

The potentiostatic cycling performance of MGC2 (Fig. 8c) showed a cathodic peak at 0.19 V, which shifted to 0.37 V in the following cycling. In the first anodic process, a main peak was located at 1.23 V, corresponding to the electrochemical oxidation of Mn(0) to Mn(II). There was another small peak at ca. 2.1 V, which reflected the re-oxidized of Mn(II) to a higher oxidation. It is worth pointing out that this peak became less evident upon cycling, which is quite different from that of MGC1 (as shown in Fig. 7c). It is inferred that the reaction kinetics and the synergistic effects of carbon and MnO in MGC2 is not as good as that in MGC1.

According to the morphology and the component analysis mentioned above, the different performance may be due to the fact that MnO nanoparticles are dispersed homogeneously on the graphene skeleton in MGC1, and so the aggregation of these active MnO nanoparticles can be effectively prevented. Furthermore, more graphene in MGC1 enhanced the electrical conductivity, the chemical stability and the synergistic effects of the components in the active electrode materials. Additionally, higher specific surface area of MGC1 also benefits lithium ion and electron transport. Thus, utilization efficiency of MnO during the lithiation and delithiation is largely enhanced, although the capacity of MGC1 is still not high enough under high current densities, which may be due to the fact that the graphene component in the composite has significant defects arising from the thermal reduction of graphene oxide[54, 55] and thus the electrical conductivity is not as high as pristine graphene.[56] While for MGC2, the graphene content is much lower as compared to that in MGC1, which leads to poor electronic conductivity and severe aggregation of MnO as shown in TEM images, thus the performance is not as good as that of MGC1.

To prove the important effect of graphene content, electrochemical impedance spectroscopy (EIS) measurement was also carried out with the frequency ranging from 100 kHz to 100 mHz using fresh batteries. Fig. 9 shows the Nyquist plots of MGC1 and MGC2 without any discharge/charge cycles, which are similar and composed of one semicircle and an inclined line, indicative of diffusion. The diameter of the semicircle reflects the resistance of the charge-transfer reaction at the electrode/electrolyte interface while the slope line is related with the Warburg impedance originated from the diffusion of lithium ions in the electrode. It is obvious that MGC1 electrode exhibits a much lower resistance than MGC2, proving that MnO well-dispersed on graphene displayed improved conductivity and discharge/charge kinetics.

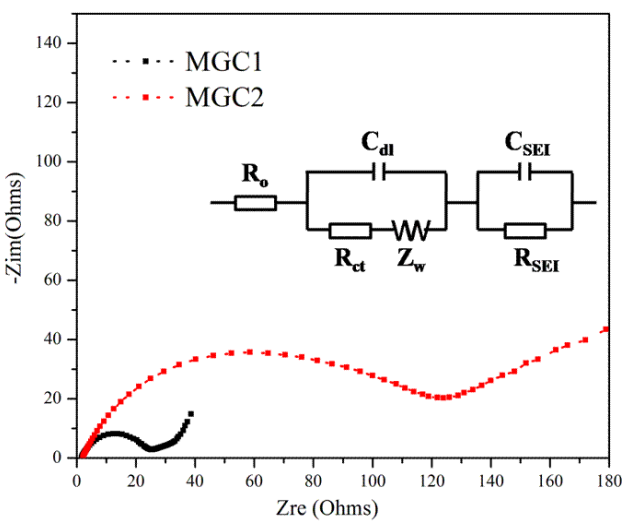

Figure 9. Electrochemical impedance spectra of the MnO/rGO composites.

Conclusions

In summary, a novel approach for fabricating MnO/rGO composites was introduced for the first time by utilizing the reducting power of graphene oxide during the thermolysis of precursors, i.e., MnO_2/graphene oxide composites. CO releasing out from the graphene oxide can successfully reduce MnO_2 to form MnO while graphene oxide was reduced partially to form rGO, thus no reducing gas or agent is used during the calcination. By controlling the ratio of initial reactants ($KMnO_4$ and graphene oxide), the component of the MnO_2/graphene oxide composites can be tuned, then further leading to different composed MnO/rGO composites, noted as MGC1 and MGC2, both of which were applied as active material for lithium ion batteries. MGC1 showed a superior cycling performance and lithium-storage capacity. Under 100 and 200 mA g^{-1}, MGC1 could deliver reversible capacities as high as 900 and 750 mAh g^{-1}, respectively after more than 100 cycles. In consideration of the simple and low-cost synthesis process, it is quite promising to apply the composites for practical manufacture. The results also contribute a lot for the extension of graphene oxide in synthesizing other functional materials due to the first utilization of its reducing power in the thermolysis.

Acknowledgment

The authors acknowledge the financial support from National Natural Science Foundation of China(21272236, 21225730, 21207136and 91326202), the Ministry of Science and Technology of China (2011CB933700) and Hefei Center for Physical Science and Technology (2012FXZY005).

Notes

[a]*School of Environment and Chemical Engineering, North China Electric Power University, Beijing 102206, P.R. China. Fax: +8655165591310; Tel: +8655165592788; E-mail: xkwang@ipp.ac.cn or xkwang@ncepu.edu.cn*

[b]*School of Chemistry, University of St Andrews, St Andrews, Fife, KY16 9ST, United Kingdom. Fax: +44 1334 463808; Tel: +441334463817; E-mail: jtsi@st-andrews.ac.uk*

[c]*Faculty of Engineering, King Abdulaziz University, Jeddah 21589, Saudi Arabia*

[d]*School for Radiological and Interdisciplinary Sciences, Soochow University, 215123, Suzhou, P. R. China*

[e]*Collaborative Innovation Center of Radiation Medicine of Jiangsu Higher Education Institutions, P. R. China*

† Electronic Supplementary Information (ESI) available: Material synthesis and characterization, electrochemical measurements, XRD patterns of the precursors, component analysis of precursors and final products by TGA and N_2 adsorption/desorption isotherms of MGC1 and MGC2. See DOI: 10.1039/b000000x/

‡ The manuscript was written through contributions of all authors. All authors have given approval to the final version of the manuscript. The authors declare no competing financial interest.

References

1. A. Magasinski, P. Dixon, B. Hertzberg, A. Kvit, J. Ayala and G. Yushin, *Nat. Mater.*, 2010, **9**, 353-358.
2. L.-X. Yuan, Z.-H. Wang, W.-X. Zhang, X.-L. Hu, J.-T. Chen, Y.-H. Huang and J. B. Goodenough, *Energy Environ. Sci.*, 2011, **4**, 269-284.
3. C. K. Chan, H. Peng, G. Liu, K. McIlwrath, X. F. Zhang, R. A. Huggins and Y. Cui, *Nat. Nanotechnol.*, 2008, **3**, 31-35.
4. K. Kang, Y. S. Meng, J. Bréger, C. P. Grey and G. Ceder, *Science*, 2006, **311**, 977-980.
5. H. Li, Z. Wang, L. Chen and X. Huang, *Adv. Mater.*, 2009, **21**, 4593-4607.
6. J. S. Chen, Y. L. Cheah, Y. T. Chen, N. Jayaprakash, S. Madhavi, Y. H. Yang and X. W. Lou, *J. Phys. Chem. C*, 2009, **113**, 20504-20508.
7. X. W. Lou, J. S. Chen, P. Chen and L. A. Archer, *Chem. Mater.*, 2009, **21**, 2868-2874.
8. X. W. Lou, C. M. Li and L. A. Archer, *Adv. Mater.*, 2009, **21**, 2536-2539.
9. J. S. Chen, Y. L. Tan, C. M. Li, Y. L. Cheah, D. Luan, S. Madhavi, F. Y. C. Boey, L. A. Archer and X. W. Lou, *J. Am. Chem. Soc.*, 2010, **132**, 6124-6130.
10. Y. Sun, X. Hu, W. Luo and Y. Huang, *ACS Nano*, 2011, **5**, 7100-7107.
11. Y. Sun, X. Hu, J. C. Yu, Q. Li, W. Luo, L. Yuan, W. Zhang and Y. Huang, *Energy Environ. Sci.*, 2011, **4**, 2870-2877.
12. O. Ghodbane, J.-L. Pascal and F. d. r. Favier, *ACS Appl. Mater. Interfaces*, 2009, **1**, 1130-1139.
13. Z. Lei, F. Shi and L. Lu, *ACS Appl. Mater. Interfaces*, 2012, **4**, 1058-1064.
14. P. Poizot, S. Laruelle, S. Grugeon, L. Dupont and J. M. Tarascon, *Nature*, 2000, **407**, 496-499.
15. X. Fang, X. Lu, X. Guo, Y. Mao, Y.-S. Hu, J. Wang, Z. Wang, F. Wu, H. Liu and L. Chen, *Electrochem. Commun.*, 2010, **12**, 1520-1523.
16. S. Laruelle, S. Grugeon, P. Poizot, M. Dolle, L. Dupont and J. Tarascon, *J. Electrochem. Soc.*, 2002, **149**, A627-A634.
17. H. Li, P. Balaya and J. Maier, *J. Electrochem. Soc.*, 2004, **151**, A1878-A1885.
18. M.-S. Wu, Y.-H. Ou and Y.-P. Lin, *Electrochim. Acta*, 2010, **55**, 3240-3244.
19. K. M. Nam, J. H. Shim, D.-W. Han, H. S. Kwon, Y.-M. Kang, Y. Li, H. Song, W. S. Seo and J. T. Park, *Chem. Mater.*, 2010, **22**, 4446-4454.
20. J. Xiang, J. Tu, Y. Yuan, X. Huang, Y. Zhou and L. Zhang, *Electrochem. Commun.*, 2009, **11**, 262-265.
21. J. Fan, T. Wang, C. Yu, B. Tu, Z. Jiang and D. Zhao, *Adv. Mater.*, 2004, **16**, 1432-1436.

22. F. Cheng, Z. Tao, J. Liang and J. Chen, *Chem. Mater.*, 2007, **20**, 667-681.

23. J. Guo, Q. Liu, C. Wang and M. R. Zachariah, *Adv. Func. Mater.*, 2012, **22**, 803-811.

24. H. Xia, M. Lai and L. Lu, *J. Mater. Chem.*, 2010, **20**, 6896-6902.

25. A. L. M. Reddy, M. M. Shaijumon, S. R. Gowda and P. M. Ajayan, *Nano Lett.*, 2009, **9**, 1002-1006.

26. Y. Ding, C. Wu, H. Yu, J. Xie, G. Cao, T. Zhu, X. Zhao and Y. Zeng, *Electrochim. Acta*, 2011, **56**, 5844-5848.

27. L. Ji and X. Zhang, *Electrochem. Commun.*, 2009, **11**, 795-798.

28. Y. Sun, X. Hu, W. Luo, F. Xia and Y. Huang, *Adv. Func. Mater.*, 2012, **23**, 2436-2444.

29. K. Zhang, P. Han, L. Gu, L. Zhang, Z. Liu, Q. Kong, C. Zhang, S. Dong, Z. Zhang and J. Yao, *ACS Appl. Mater. Interfaces*, 2012, **4**, 658-664.

30. A. Yu, H. W. Park, A. Davies, D. C. Higgins, Z. Chen and X. Xiao, *J. Phys. Chem. Lett.*, 2011, **2**, 1855-1860.

31. Y. Sun, X. Hu, W. Luo, F. Xia and Y. Huang, *Adv. Func. Mater.*, 2013, **23**, 2436-2444.

32. K. J. Zhang, P. X. Han, L. Gu, L. X. Zhang, Z. H. Liu, Q. S. Kong, C. J. Zhang, S. M. Dong, Z. Y. Zhang, J. H. Yao, H. X. Xu, G. L. Cui and L. Q. Chen, *ACS Appl. Mater. Interfaces*, 2012, **4**, 658-664.

33. X. Li, S. Xiong, J. Li, X. Liang, J. Wang, J. Bai and Y. Qian, *Chem. Eur. J.*, 2013, **19**, 11310-11319.

34. I. Jung, D. Dikin, S. Park, W. Cai, S. L. Mielke and R. S. Ruoff, *J. Phys. Chem. C*, 2008, **112**, 20264-20268.

35. R. Larciprete, S. Fabris, T. Sun, P. Lacovig, A. Baraldi and S. Lizzit, *J. Am. Chem. Soc.*, 2011, **133**, 17315-17321.

36. G. Zhao, J. Li, L. Jiang, H. Dong, X. Wang and W. Hu, *Chem. Sci.*, 2012, **3**, 433-437.

37. J. F. Moulder, W. F. Stickle, P. E. Sobol and K. D. Bomben, Perkin-Elmer: Boca Raton, FL, 1992.

38. A. A. Audi and P. Sherwood, *Surf.Interface Anal.*, 2002, **33**, 274-282.

39. T. W. Kim, H. Yoo, I. Y. Kim, H. W. Ha, A. R. Han, J. S. Chang, J. S. Lee and S. J. Hwang, *Adv. Func. Mater.*, 2011, **21**, 2301-2310.

40. M. Wei, Y. Konishi, H. Zhou, H. Sugihara and H. Arakawa, *Nanotechnology*, 2005, **16**, 245.

41. M. Polverejan, J. C. Villegas and S. L. Suib, *J. Am. Chem. Soc.*, 2004, **126**, 7774-7775.

42. A. H. Reidies, in *Ullmann's Encyclopedia of Industrial Chemistry*, Wiley-VCH Verlag GmbH & Co. KGaA, 2000.

43. Y. Hou, Y. Cheng, T. Hobson and J. Liu, *Nano Lett.*, 2010, **10**, 2727-2733.

44. S. Q. Wang, J. Y. Zhang and C. H. Chen, *J. Power Sources*, 2010, **195**, 5379-5381.

45. D. Y. Pan, S. Wang, B. Zhao, M. H. Wu, H. J. Zhang, Y. Wang and Z. Jiao, *Chem. Mater.*, 2009, **21**, 3136-3142.

46. P. C. Lian, X. F. Zhu, S. Z. Liang, Z. Li, W. S. Yang and H. H. Wang, *Electrochim. Acta*, 2010, **55**, 3909-3914.

47. B. Sun, Z. X. Chen, H. S. Kim, H. Ahn and G. X. Wang, *J. Power Sources*, 2011, **196**, 3346-3349.

48. O. Delmer, P. Balaya, L. Kienle and J. Maier, *Adv. Mater.*, 2008, **20**, 501-505.

49. J. Liu and Q. Pan, *Electrochem. Solid-State Lett.*, 2010, **13**, A139-A142.

50. K. Zhong, X. Xia, B. Zhang, H. Li, Z. Wang and L. Chen, *J. Power Sources*, 2010, **195**, 3300-3308.

51. H. Wang, L.-F. Cui, Y. Yang, H. Sanchez Casalongue, J. T. Robinson, Y. Liang, Y. Cui and H. Dai, *J. Am. Chem. Soc.*, 2010, **132**, 13978-13980.

52. J. Gao, M. A. Lowe and H. D. Abruña, *Chem. Mater.*, 2011, **23**, 3223-3227.

53. J. Guo, Q. Liu, C. Wang and M. R. Zachariah, *Adv. Func. Mater.*, 2012, **22**, 803-811.

54. C. Gómez-Navarro, J. C. Meyer, R. S. Sundaram, A. Chuvilin, S. Kurasch, M. Burghard, K. Kern and U. Kaiser, *Nano Lett.*, 2010, **10**, 1144-1148.

55. G. Lu, L. E. Ocola and J. Chen, *Appl. Phys. Lett.*, 2009, **94**, 083111-083111-083113.

56. S. Stankovich, D. A. Dikin, R. D. Piner, K. A. Kohlhaas, A. Kleinhammes, Y. Jia, Y. Wu, S. T. Nguyen and R. S. Ruoff, *Carbon*, 2007, **45**, 1558-1565.

TOC